International Journal of Design & Nature and Ecodynamics
Vol. 21, No. 1, January, 2026, pp. 195-205
Journal homepage: http://iieta.org/journals/ijdne

Green Synthesis of Fe_2O_3@Ag/AgCl Core–Shell Nanoparticles with Different $AgNO_3$ Concentrations for Enhanced Photocatalytic Degradation of Methylene Blue Under UV Irradiation

Ruqayah A. Ulwali, Nada K. Abbas*

Department of Physics, College of Science for Women, University of Baghdad, Baghdad 10071, Iraq

Corresponding Author Email: nadaka_phys@csw.uobaghdad.edu.iq

https://doi.org/10.18280/ijdne.210118

Received: 10 November 2025
Revised: 20 January 2026
Accepted: 27 January 2026
Available online: 31 January 2026

Keywords:
green synthesis, Fe_2O_3@Ag/AgCl core-shell NPs, photocatalytic degradation, methylene blue dye

ABSTRACT

In this study, Fe_2O_3@Ag/AgCl core–shell nanoparticles were synthesized using mint leaf extract via a green synthesis approach. Two concentrations of silver nitrate ($AgNO_3$) (0.02 and 0.03 M) were used to investigate the effect of silver content on the structural, morphological, and optical properties. X-ray diffraction (XRD) confirmed the formation of the hematite phase (α-Fe_2O_3) along with metallic silver (Ag) and silver chloride (AgCl); increasing the $AgNO_3$ concentration improved crystallinity and reduced crystallite size. Energy-dispersive X-ray spectroscopy (EDX) showed increased silver and chlorine contents at the higher precursor concentration. Transmission electron microscopy (TEM) revealed spherical nanoparticles with an Ag/AgCl shell, which became thicker as the $AgNO_3$ concentration increased. Fourier-transform infrared spectroscopy (FTIR) confirmed the presence of organic functional groups from the plant extract acting as stabilizing agents, in addition to bands corresponding to Fe–O bonds. Atomic force microscopy (AFM) indicated differences in surface roughness and particle compactness, with the 0.03 M sample exhibiting a more uniform and denser surface. Moreover, ultraviolet–visible (UV–Vis) spectroscopy showed enhanced absorption and a change in the optical band gap with increasing silver content, with band-gap values of 3.33 and 3.50 eV. Photocatalytic tests demonstrated that Fe_2O_3@Ag/AgCl prepared with 0.03 M $AgNO_3$ (3 mg catalyst dose) was the most effective for methylene blue degradation under ultraviolet irradiation, with degradation increasing over exposure times of 15, 30, 45, and 60 min. Finally, pseudo-first-order kinetic analysis showed that Fe_2O_3@Ag/AgCl (0.03 M) achieved a higher apparent rate constant (K_{app} = 0.02445 min^{-1}, R^2 = 0.8698) than Fe_2O_3@Ag/AgCl (0.02 M) (K_{app} = 0.01937 min^{-1}, R^2 = 0.9097).

1. INTRODUCTION

Nanotechnology has gained considerable attention in recent years due to its potential applications in medicine, catalysis, and environmental remediation (this includes the photodegradation of organic pollutants) [1]. Among these pollutants, methylene blue is a widely used dye in the textile and chemical industries that has caused water and environmental pollution due to its resistance to conventional biodegradation [2]. Photocatalysis using nanomaterials is therefore one of the most effective solutions for removing these dyes because of the high light absorption capacity of these materials and their ability to produce reactive oxygen species (ROS), which contribute to the breakdown of the dye molecules [3]. Among the various types of nanomaterials, iron oxide nanoparticles (Fe_2O_3 NPs) are of particular interest because of their excellent biocompatibility, magnetic properties, and chemical stability [4]. Specifically, α-Fe_2O_3 (hematite), the most thermodynamically stable phase of iron oxide under ambient conditions, it is an n-type semiconductor with a narrow band gap (~ 2.1 eV), enabling efficient light absorption in the visible region [5, 6]. Moreover, α-Fe_2O_3 possesses weak ferromagnetic properties at room temperature and excellent corrosion resistance, which make it highly suitable for catalytic, magnetic, and biomedical applications [7]. Hybrid nanostructures such as Fe_2O_3@Ag/AgCl core–shell nanoparticles have been developed, combining the unique physicochemical and biological features of iron oxide with silver and silver chloride [8]. The synergistic interaction between the core and shell components enhances charge separation, surface reactivity, and biological efficacy [9]. Traditional synthesis methods of such nanoparticles often involve toxic chemicals, high temperatures, and complex procedures, which can limit their biomedical applications due to potential toxicity and environmental hazards [10]. Therefore, green synthesis approaches have emerged as eco-friendly and sustainable alternatives, utilizing plant extracts as natural reducing and stabilizing agents [11]. Plant-based synthesis is cost-effective, simple, and environmentally benign, with phytochemicals such as polyphenols, flavonoids, and alkaloids playing a vital role in reducing metal ions and capping the resulting nanoparticle [12]. In this study,

Fe_2O_3@Ag/AgCl core–shell nanoparticles were synthesized using mint leaf extract at two different concentrations of silver nitrate, the concentration of $AgNO_3$ is a crucial factor in green synthesis because it determines the amount of silver ions available during the reaction, which controls the formation of the Ag/AgCl shell around the Fe_2O_3 NPs in terms of thickness, regularity, and surface coverage. This, in turn, affects the optical properties of the material by enhancing light absorption and the surface plasmon effect of silver. It also helps improve charge separation and reduce electron and hole recombination, ultimately leading to enhanced photocatalytic efficiency in the decomposition of methylene blue dye.

2. PREPARATION METHOD AND EXPERIMENTAL PART

2.1 Materials used in preparation

Mint leaves (*Mentha spicata* species) purchased from local markets, iron nitrate $Fe(NO_3)_3$ $9H_2O$ (Daryaganj, Delhi, India, 98%), silver nitrate $AgNO_3$ (CDH, India, 99.9%), deionized water (DW), and ethanol (96%).

2.2 Preparation of Fe_2O_3@Ag/AgCl core shell NPs

Fe_2O_3@Ag/AgCl core-shell was prepared using the green method, with modifications, as described in the study by Sarani et al. [13]. 10 grams of mint leaves were used after washing and drying, and then 250 mL of DW was added to them, and then heated at 60°C for 1 h. The resulting extract was filtered and cooled to room temperature. First, 30 mL of mint leaf extract was added to 0.1 M of $Fe(NO_3)_3$ $9H_2O$ dissolved in 50 mL of DW with continuous stirring under a magnetic stirrer drop by drop at room temperature. Then, silver nitrate at concentrations of 0.02 and 0.03 M was added, dissolved in 50 mL of deionized water, and the reaction continued for one hour. The resulting precipitate was separated using a centrifuge for 30 min at 4000 rpm. The precipitate was then washed twice with DW and once with ethanol, each time for 30 min, leaving a black precipitate. Finally, the precipitate was annealed at 600°C for 3 hours. Figure 1 represents the steps for preparing Fe_2O_3 @Ag/AgCl core-shell NPs using the green method.

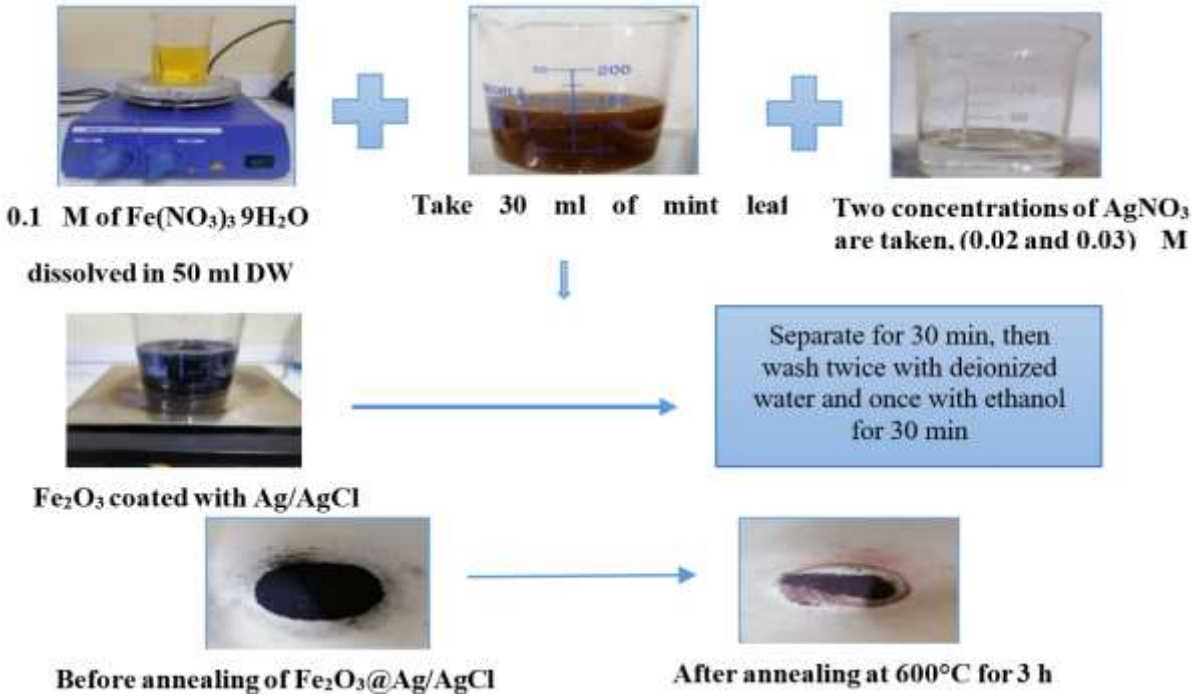

Figure 1. The steps for preparing Fe_2O_3@Ag/AgCl core-shell NPs using the green method

2.3 The test of photocatalytic activity of Fe_2O_3@Ag/AgCl core-shell NPs for the degradation of methylene blue dye

2.3.1 Irradiation system

The irradiation device was produced in a laboratory as a box housing two ultraviolet (UV) lamps (broad-spectrum, 320–400 nm), with each having an energy output of 10 watts. The two bulbs were put in tandem inside the inner covering of the closed box, with a separation of 5 cm between them. The samples were positioned 15 cm above the UV light.

2.3.2 Photocatalytic experiment

The photocatalytic experiment was conducted using Fe_2O_3@Ag/AgCl core-shell NPs as a catalyst by first dissolving 3 mg of methylene blue dye in 1 L of distilled water (0.003 g/L). Subsequently, 3 mg of the catalyst material was added to 15 mL of the dye solution, corresponding to a catalyst dosage of (0.2 g/L), and stirred to ensure adsorption/desorption equilibrium of the dye on the catalyst surface before exposure to UV light. The solution was then irradiated with a UV lamp for different time intervals (15, 30, 45, and 60 minutes). After each exposure period, the dye solution was filtered using filter paper, and the absorbance of the dye was measured using a UV–visible spectrophotometer (Shimadzu UV-1800 spectrophotometer), λ= 400-800 nm, recording the absorbance before irradiation (considered as A_0) and after irradiation (A_t). The degree of dye degradation (D%) was then calculated using the following relation [14]:

$$D\ (\%) = (A_0 - A_t)/A_0 \quad (1)$$

2.4 Characterization techniques

Sample characterization was performed using a combination of measurement techniques. X-ray diffraction (XRD) was conducted within an (2θ = 5-80°) angular range at a typical scanning rate of 2°/min using a Cu Kα source. Nanostructure was investigated using TEM at an acceleration voltage of 120 kV. Elemental analysis was performed using Energy-dispersive X-ray spectroscopy (EDX) at a spectral resolution of 129 eV to determine the chemical composition of the elements. Additionally, Fourier-transform infrared spectroscopy (FTIR) was used within a spectral range of 4000–400 cm^{-1} and a resolution of 4 cm^{-1} to analyze functional groups. Surface topography was analyzed using atomic force microscopy (AFM) within a scanning range of up to 100 × 100 µm to obtain three-dimensional images and measurements of roughness and grain size. As for the optical properties, they were studied using an ultraviolet-visible (UV-Vis) spectrometer within a wavelength range of 190–1100 nm with an appropriate integration time for each scan to ensure the accuracy of the measurements and reduce spectral noise.

3. RESULTS AND DISCUSSION

3.1 Crystallographic analysis (XRD)

XRD patterns of Fe_2O_3@Ag/AgCl NPs prepared with two different silver nitrate concentrations (0.02 and 0.03 M) indicate a clear effect of concentration on the structure and crystallinity of the material. Fe_2O_3@Ag/AgCl (Figure 2(a)) with a lower silver nitrate concentration shows less sharp and lower intensity peaks compared to Fe_2O_3@Ag/AgCl (Figure 2(b)) with a higher concentration after annealing at 600°C, as shown in Figure 2. These peaks are due to α-Fe_2O_3, AgCl, and Ag with a hexagonal structure and a cubic structure corresponding to JCPDS card 96-900-0140, JCPDS card No. (01-085-1355) and (98-005-3759), respectively [15, 16]. The appearance of silver chloride (AgCl) in the samples, especially since it was not directly used in the reaction, is attributed to the use of mint leaf extract, which contains organic compounds and natural salts including chloride ions (Cl^-), AgCl forms initially as a surface-associated phase, while Fe_2O_3 crystallizes during calcination to form the core, followed by stabilization of Ag/AgCl as the shell [17].

The average crystal size of Fe_2O_3, Ag, and AgCl NPs for Fe_2O_3@Ag/AgCl NPs (0.02 M) was calculated using Eq. (2) [18] and found to be 27.43, 51.98, and 27.67 nm, respectively. In contrast, for Fe_2O_3@Ag/AgCl NPs with 0.03 M, the corresponding crystallite sizes decreased to 17.82, 23.69, and 19.46 nm for Fe_2O_3, Ag, and AgCl, respectively. This is in agreement with V. Madhubala and T. Kalaivani with increasing molar concentration of the shell, the crystal size decreases, and crystallinity increases [19]. The reduction in crystallite size with increasing shell concentration can be explained by enhanced nucleation and early surface passivation, which suppress further crystal growth and improve crystallinity [20]. Table 1(a and b) shows the structural parameters of Fe_2O_3@Ag/AgCl NPs with $AgNO_3$ (0.02 and 0.03 M).

$$D = K \lambda / \beta \cos \theta \quad (2)$$

where,

D: Mean crystallite size

K: Scherrer constant (typically 0.9)

λ: Wavelength of the X-ray (1.5418 Å)

β: Full width at half maximum (FWHM)

θ: Bragg diffraction angle (in degrees)

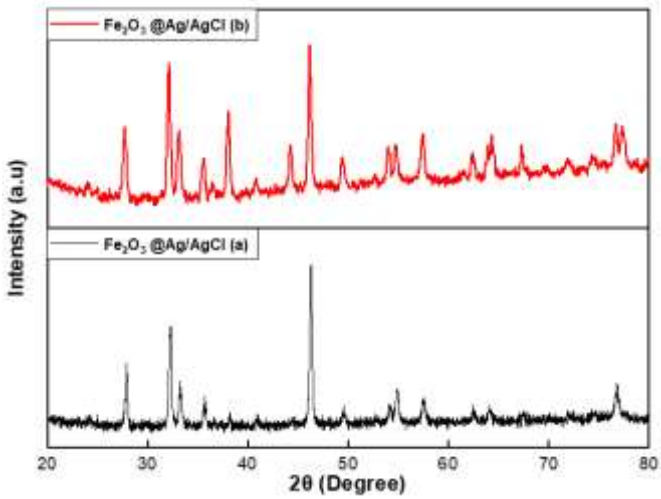

Figure 2. XRD pattern of Fe_2O_3@Ag/AgCl (a) with a lower concentration of silver nitrate (0.02 M) and Fe_2O_3@Ag/AgCl (b) with a higher concentration of silver nitrate (0.03 M)

3.2 Morphological and elemental analysis (TEM, EDX)

The TEM image, Figure 3(A) for Fe_2O_3@Ag/AgCl NPs, with 0.02M of $AgNO_3$, shows that the particles form a regular spherical shape, with a thin Ag/AgCl coating around the iron oxide [13]. In the TEM image (Figure 3(B)), with 0.03 M of $AgNO_3$, a thicker Ag/AgCl coating forms around the particles. This excess coating causes an increased deposition density and slight irregularity in the spherical shape of the particles, although the overall shape remains spherical, making the particles in image B less regular than in image A [21].

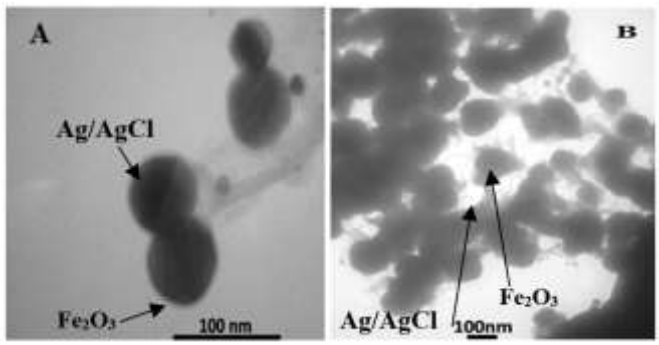

Figure 3. TEM images of Fe_2O_3@Ag/AgCl nanoparticles (NPs) prepared with $AgNO_3$ concentrations of (A) 0.02 M and (B) 0.03 M

Also, EDX analysis reveals, as shown in Figure 4(A and B), that the differences between the Fe_2O_3@Ag/AgCl NPs are primarily due to the effect of silver nitrate concentration on the reaction, as well as the use of mint leaf extract in the preparation. The weight and atomic percentages of the elements are shown in Table 2(a and b), where the silver nitrate concentration is low (0.02 M), silver and chloride are present in lower ratios, along with iron and oxygen, resulting in a thin Ag/AgCl coating around the iron oxide. However, when a higher silver nitrate concentration (0.03 M) is used, silver and

chloride precipitation increase, as well as the presence of iron and oxygen, leading to a thicker Ag/AgCl coating [22]. Additionally, the presence of other elements from the plant extract, such as Si, Al, P, and S, was observed, indicating traces of organic compounds present in the extract [23].

Table 1a. The structural parameters of Fe_2O_3@Ag/AgCl NPs with 0.02 M of $AgNO_3$

2θ (Deg.)	FWHM (Deg.)	dhkl Exp.(Å)	C.S (nm)	hkl	Phase
33.2	0.341	2.695	24.29	(104)	α-Fe_2O_3
35.6	0.227	2.514	36.72	(110)	α-Fe_2O_3
40.9	0.293	2.200	28.86	(113)	α-Fe_2O_3
49.541	0.416	1.838	21.02	(20$\bar{4}$)	α-Fe_2O_3
54.887	0.420	1.671	21.28	(116)	α-Fe_2O_3
57.538	0.479	1.600	18.90	(21$\bar{2}$)	α-Fe_2O_3
62.521	0.218	1.484	42.60	(214)	α-Fe_2O_3
64.127	0.363	1.451	25.77	(300)	α-Fe_2O_3
38.200	0.161	2.354	51.98	(111)	Ag
27.915	0.21198	3.193	38.64	(111)	AgCl
32.315	0.348	2.768	23.77	(200)	AgCl
46.296	0.298	1.959	28.94	(220)	AgCl
76.766	0.523	1.240	19.35	(420)	AgCl

Table 1b. The structural parameters of Fe_2O_3@Ag/AgCl NPs with 0.03 M of $AgNO_3$

2θ (Deg.)	FWHM (Deg.)	dhkl Exp.(Å)	C.S (nm)	hkl	Phase
33.140	0.442	2.7010	18.74	(104)	α-Fe_2O_3
35.571	0.380	2.5218	21.93	(110)	α-Fe_2O_3
49.266	0.498	1.8481	17.55	(20$\bar{4}$)	α-Fe_2O_3
54.678	0.493	1.6773	18.11	(116)	α-Fe_2O_3
57.461	0.504	1.6025	17.95	(21$\bar{2}$)	α-Fe_2O_3
62.433	0.474	1.4863	19.57	(214)	α-Fe_2O_3
64.358	0.861	1.4464	10.90	(300)	α-Fe_2O_3
38.046	0.370	2.3632	22.68	(111)	Ag
44.184	0.347	2.0481	24.71	(002)	Ag
27.717	0.433	3.2159	18.90	(111)	AgCl
32.128	0.326	2.7837	25.30	(200)	AgCl
46.131	0.363	1.9661	23.75	(220)	AgCl
67.262	0.437	1.3908	21.83	(400)	AgCl
76.689	1.343	1.2416	7.54	(420)	AgCl

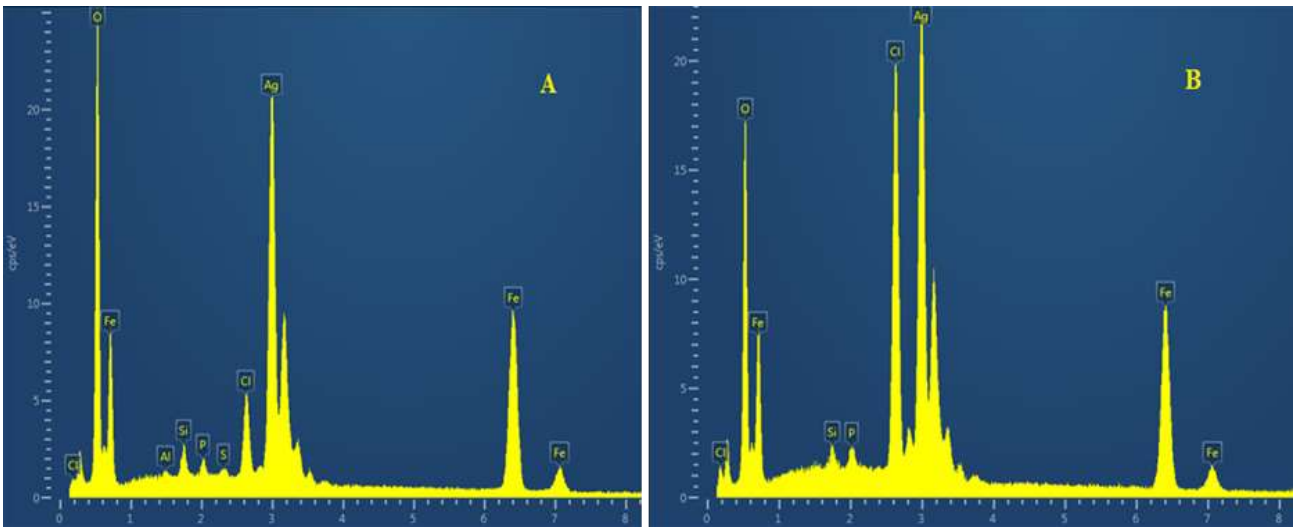

Figure 4. EDX spectra of Fe_2O_3@Ag/AgCl nanoparticles (NPs) prepared with silver nitrate ($AgNO_3$) concentrations of (A) 0.02 M and (B) 0.03 M

3.3 Surface functional group analysis (FTIR)

The two FTIR spectra presented in Figure 5 reflect the effect of different silver nitrate concentrations in the preparation of Fe_2O_3@AgAgCl using mint leaf extract. The peaks at 3436.34 cm^{-1} and 3435.79 cm^{-1} appear in the Fe_2O_3@AgAgCl (Figure 5(a and b)) spectra, respectively, indicating the presence of hydrogen bonds or adsorbed water on the surface of the particles [24]. While the peaks at 2957.11 cm^{-1}, 2924.59 cm^{-1},2853.87 cm^{-1} and 2957.02 cm^{-1}, 2924.31 cm^{-1},2853.72 cm^{-1} reflect the presence of extended C–H bonds, indicating the presence of hydrocarbon groups in the plant extract, and contribute to this enhanced organic interaction [25]. The peaks at 1740.97 cm^{-1} and 1741.16 cm^{-1} also appear, indicating the

presence of C=O bonds in the organic compounds derived from the extract [26]. The peaks at 1632.01 cm^{-1} and 1632.02 cm^{-1} represent unsaturated C=C bonds, reflecting the organic effect of the extract [27]. The peaks at (1465.56 cm^{-1} and 1384.88 cm^{-1}), (1465.83 cm^{-1} and 1384.85 cm^{-1}) indicate C–H bending, reflecting the presence of methyl or ethyl groups in the organic compounds, enhancing the effect of the extract on reacting with metals [28]. The peaks at 1270.64 cm^{-1} and 1269.88 cm^{-1} represent C–O bonds, indicating the presence of oxide compounds [29]. The peaks at 1111.38 cm^{-1} and 1112.70 cm^{-1} reflect the presence of Si–O or Si–C bonds [30]. Furthermore, the presence of surface groups resulting from the plant extract components may be due to the decomposition of organic components after annealing [31].

Table 2a. The weight and atomic ratios of the elements for Fe_2O_3@Ag/AgCl NPs with silver nitrate (0.02 M)

Element	Wt%	Atomic %
O	23.08	57.06
Al	0.12	0.17
Si	0.68	0.95
P	0.43	0.55
S	0.20	0.25
Cl	2.14	2.39
Fe	34.37	24.34
Ag	38.99	14.29

Table 2b. The weight and atomic ratios of the elements for Fe_2O_3@Ag/AgCl NPs with silver nitrate (0.03 M)

Element	Wt%	Atomic %
O	17.71	47.15
Si	0.37	0.57
P	0.48	0.66
Cl	10.50	12.62
Fe	29.88	22.79
Ag	41.07	16.22

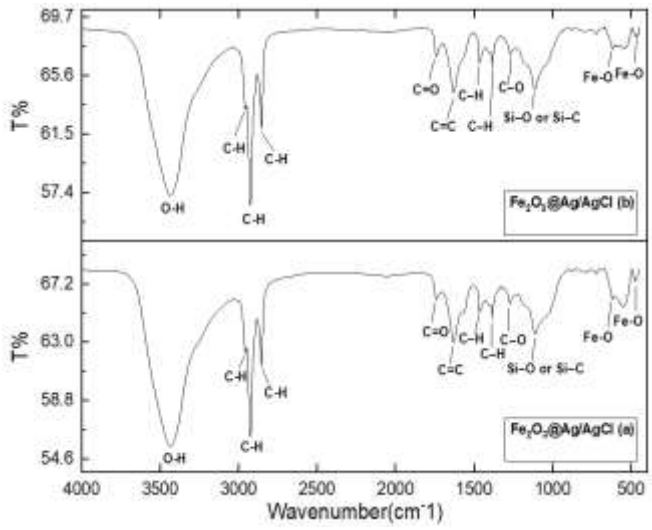

Figure 5. FTIR spectra for Fe_2O_3@Ag/AgCl (a) with (0.02 M) of silver nitrate and Fe_2O_3@Ag/AgCl (b) with (0.03 M) of silver nitrate

Finally, the peaks at 551.46 cm^{-1}, 472.03 cm^{-1}, 618.25 cm^{-1}, and 463.43 cm^{-1} reflect metallic bonds for Fe–O [32]. The spectrum for Fe_2O_3@Ag/AgCl (Figure 5(b)) indicates higher permeability, indicating a higher concentration of silver and silver chloride on the surface of the iron oxide; encapsulating the core isolates active surface sites in the Fe_2O_3 nucleus, such as surface defects and unsaturated bonds, which typically contribute to strong infrared absorption [33]. The absence of characteristic peaks for silver chloride is due to its ionic nature, which is not usually seen in FTIR [34].

3.4 Topographical analysis (AFM)

The AFM image in Figure 6(A) represents Fe_2O_3@AgAgCl NPs using 0.02 M of silver nitrate in the reaction. It shows an irregular surface with lower elevations and varying details, appearing to have rough, uneven textures, and the average particle size is 59.07 nm with roughness 23.16 nm. The AFM image in Figure 6(B), where a higher concentration of silver nitrate (0.03 M) was used, shows a more regular surface with sharp peaks and distinct shapes, indicating a more stable surface. The average particle size is 66.10 nm, and the roughness is 3.77 nm, reflecting a smoother, denser surface. This is an agreement with the study [35]. The decrease in surface roughness with increasing $AgNO_3$ concentration is attributed to the formation of an Ag/AgCl shell around the Fe_2O_3 nucleus. At higher concentrations, increased shell deposition covers surface protrusions and fills voids, resulting in a smoother surface. This behavior is consistent with TEM results showing improved shell regularity and continuity, as well as with XRD results indicating a decrease in crystal size with increasing shell concentration. This behavior is consistent with Graziani et al. [36], where increased coating deposition leads to improved surface homogeneity and a decrease in crystal size.

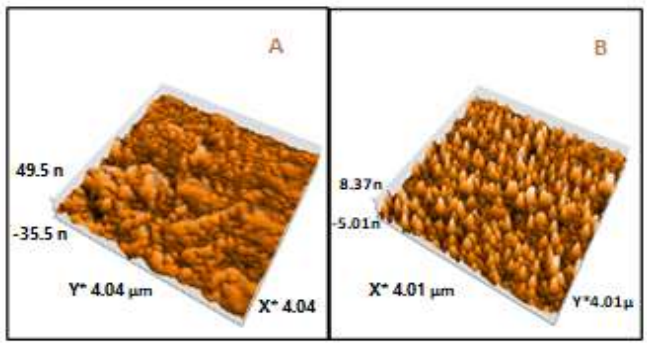

Figure 6. AFM images of Fe_2O_3@Ag/AgCl prepared with silver nitrate ($AgNO_3$) concentrations of (A) 0.02 M and (B) 0.03 M

3.5 Optical properties (UV-Vis DRS and band gap)

In this analysis, the effect of silver nitrate concentration on the properties of Fe_2O_3@Ag/AgCl was investigated using optical absorption spectroscopy and Tauc plot analysis using Eq. (3) [37]. Fe_2O_3@Ag/AgCl with a low concentration of silver nitrate (0.02 M) showed lower light absorption in the ultraviolet range, with an energy gap of 3.33 eV, as shown in Figure 7(a and b). In contrast, Fe_2O_3@Ag/AgCl with a high concentration of silver nitrate (0.03 M) showed increased light absorption in the ultraviolet range and a larger energy gap of 3.5 eV [38], as shown in Figure 7(c and d). The increase in the optical band gap with increasing silver nitrate concentration is attributed to structural and electronic changes resulting from the formation of Ag/AgCl shell around the Fe_2O_3 nucleus;

therefore, higher $AgNO_3$ concentration limits crystal growth and reduces crystal size, thus widening the band gap due to the quantum confinement effect [39]. Furthermore, the presence of Ag and AgCl phases enhances absorption characteristics in the ultraviolet range. Ag promotes absorption via a localized surface plasmon effect, while AgCl modifies the electronic structure of the composite system [40].

$$(\alpha\, hv)^r = B(hv - Eg) \quad (3)$$

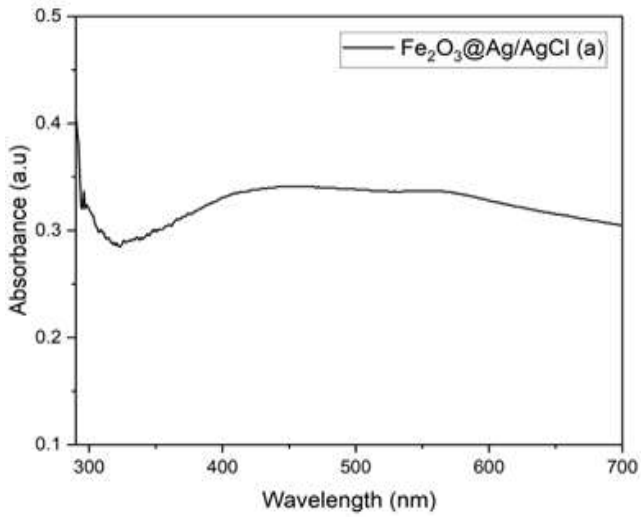

(a)

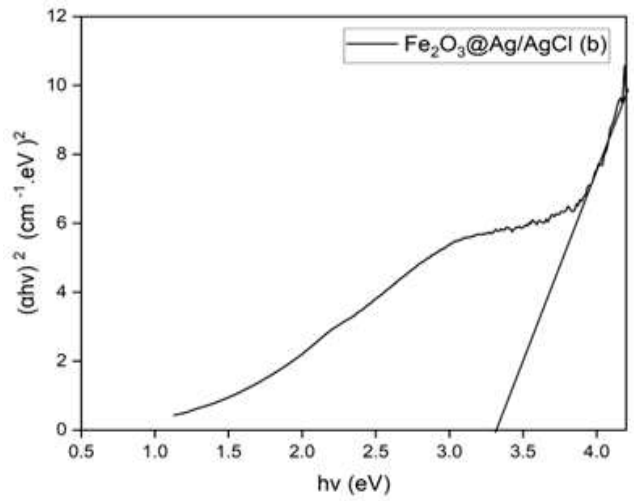

(b)

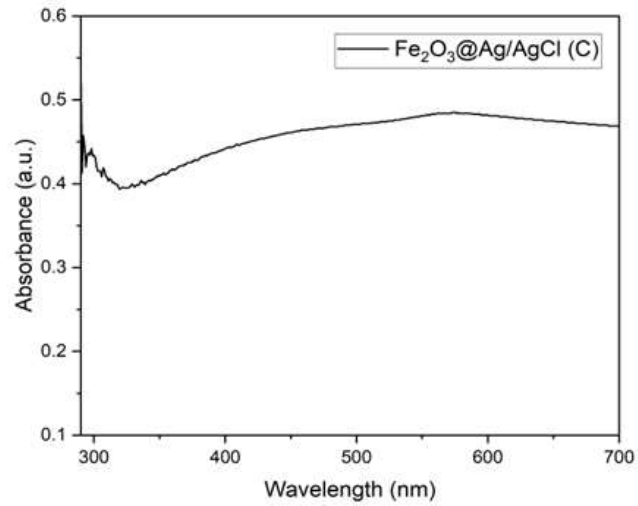

(c)

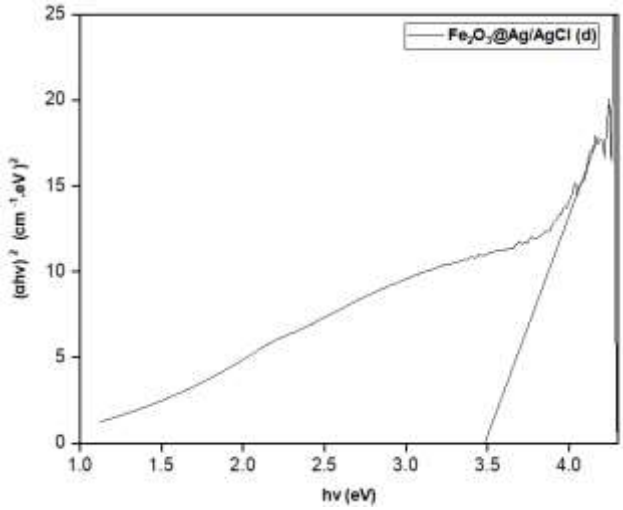

(d)

Figure 7. Optical properties of Fe_2O_3@Ag/AgCl nanoparticles (NPs): (a) UV–Vis optical absorption spectrum for Fe_2O_3@Ag/AgCl NPs prepared with 0.02 M $AgNO_3$; (b) Corresponding Tauc plot; (c) UV–Vis optical absorption spectrum for Fe_2O_3@Ag/AgCl NPs prepared with 0.03 M $AgNO_3$; (d) Corresponding Tauc plot

3.6 Photocatalytic performance of Fe_2O_3@Ag/AgCl core shell NPs

The optical absorption spectrum of methylene blue dye before and after treatment with Fe_2O_3@Ag/AgCl (0.02 and 0.03 M) and exposure to ultraviolet radiation at different times (15, 30, 45, and 60 min), as shown in the Figure 8(A and B), reveals a shift in the dye's wavelengths towards blue with increasing exposure time, particularly at 60 minutes, this may indicate to a degradation of methylene blue dye [41]. The results, as shown in Table 3a, indicate a faster and more efficient degradation (D%) of methylene blue dye when treated with Fe_2O_3@Ag/AgCl (0.03 M). The degradation rate starts at 74% after 15 minutes and reaches 92% after 60 minutes. This contrasts with the results in Table 3b for Fe_2O_3@Ag/AgCl (0.02 M), where the degradation rate (D%) starts at 70% after 15 minutes and continues to increase to 86% after 60 minutes, as shown in Figure 9(A and B), this may indicate that the increased proportion of reactants at the surface led to increased decomposition efficiency for Fe_2O_3@Ag/AgCl (0.03 M), and this is attributed to improved (e^-/h^+) separation and reduced reconnection [42].

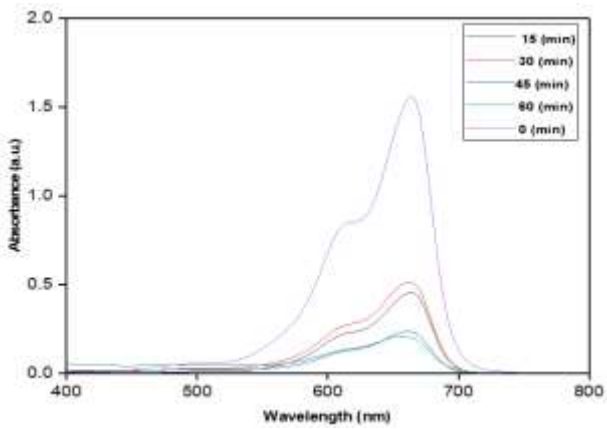

(A)

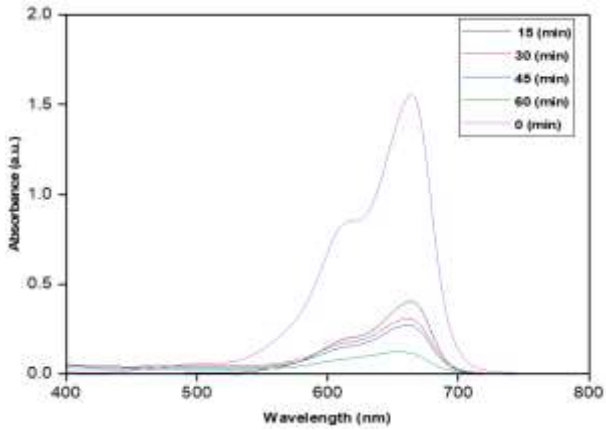

(B)

Figure 8. UV–Vis optical absorption spectra of methylene blue dye before and after treatment with Fe_2O_3@Ag/AgCl, prepared with $AgNO_3$ concentrations of (A) 0.02 M and (B) 0.03 M

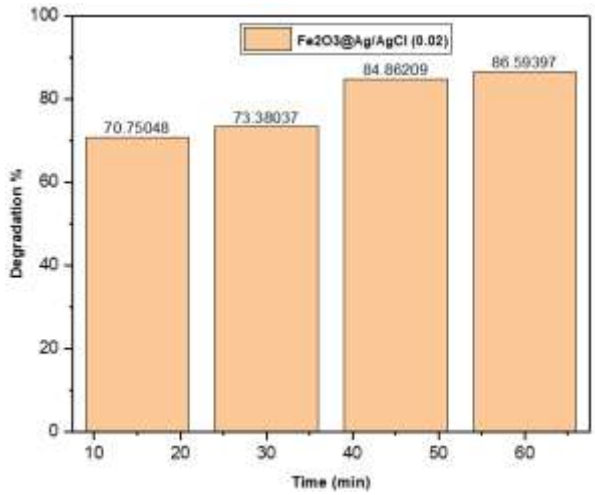

(A)

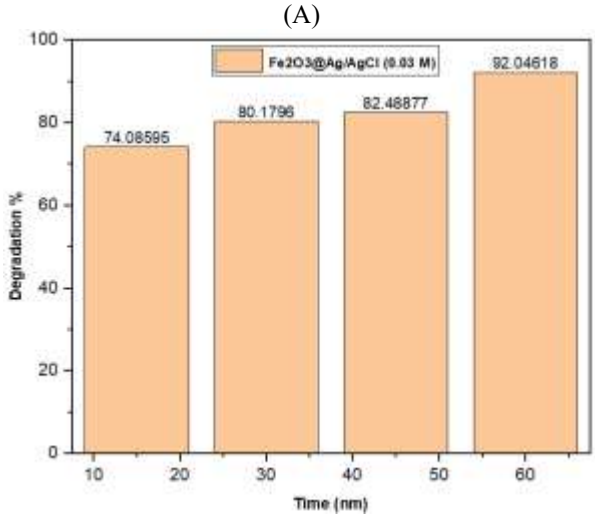

(B)

Figure 9. Decomposition efficiency of Fe_2O_3@Ag/AgCl at different exposure times (15, 30, 45, and 60 min): (A) 0.02 M and (B) 0.03 M ($AgNO_3$ precursor concentration)

To determine the concentration of dyes or the effect of reactants on the reaction rate in heterogeneous photo-oxidation systems under ultraviolet light irradiation, the Langmuir-Hinshelwood (L-H) equation is used [43].

$$Ln\left(\frac{C_t}{C_0}\right) = -K_{app}\, t \qquad (4)$$

where, t is the time in minutes, C_t is the concentration of methylene dye at time t, C_0 is the concentration before irradiation, and Kapp is the apparent reaction rate constant.

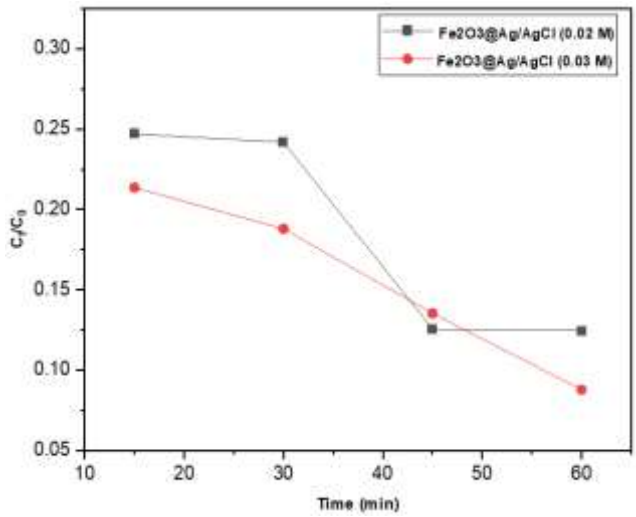

Figure 10. The concentration of methylene blue dye after UV exposure and treatment with Fe_2O_3@Ag/AgCl (0.02 M) and Fe_2O_3@Ag/AgCl (0.03 M), relative to its concentration before exposure and treatment

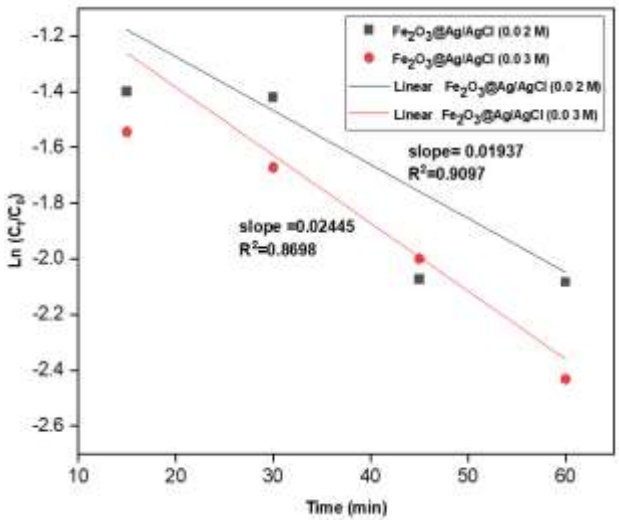

Figure 11. The slope of a straight line from the relationship between ln C_t/C_0 and time for Fe_2O_3@Ag/AgCl (0.02 and 0.03 M)

The C_t/C_0 for Fe_2O_3@Ag/AgCl (0.03 M), as shown in the Figure 10, decreases more significantly, starting at 1 (at time 0) and gradually decreasing to 0.13406 after 60 minutes, compared to Fe_2O_3@Ag/AgCl (0.02 M), where the ratio decreases from 1 to 0.079538 after 60 minutes, this indicates the Fe_2O_3@Ag/AgCl (0.03 M), was more effective at reducing the dye concentration. Therefore, the slope is calculated from the relationship between ln C_t/C_0 and time, as shown in Figure 11. The K_{app} value of Fe_2O_3@Ag/AgCl at 0.03 M was approximately 0.02445 min^{-1} with an R^2 value of 0.8698, which is higher than the K_{app} of Fe_2O_3@Ag/AgCl at 0.02 M, which was 0.01937 min^{-1} with an R^2 value of 0.9097. These

results indicate that increasing the silver nitrate concentration from 0.02 to 0.03 M accelerates the reaction and thus proves more efficient in photocatalysis. The R^2 value of 0.8698 for a 0.03 M indicates that the first-order kinetic behavior is not perfectly aligned, and the graph shows slight scattering of some points. Perhaps this is due to the increased Ag/AgCl loading, which may contribute to effects such as adsorption, light blocking/scattering, or partial aggregation, resulting in slight nonlinearity.

3.7 Photocatalytic mechanism

The structural and electronic synergy between the Fe_2O_3 core and the Ag/AgCl shell. Upon light irradiation, the Fe_2O_3 core absorbs photons and generates electron–hole pairs through the transition of electrons from the valence band to the conduction band. Owing to the core–shell architecture, the photogenerated electrons readily migrate toward the Ag shell, where metallic Ag acts as an electron sink, thereby suppressing electron–hole recombination and prolonging the lifetime of the charge carriers [44].

The electrons accumulated on the Ag surface subsequently react with adsorbed oxygen molecules to form superoxide radicals ($\bullet O_2^-$), while the remaining holes in the valence band of the Fe_2O_3 core react with water molecules or hydroxyl ions to generate hydroxyl radicals ($\bullet OH$) [45]. The presence of AgCl further contributes to modifying the electronic structure of the composite system and promoting efficient charge separation, in addition to enhancing the generation of reactive oxidizing species [46]. These $\bullet OH$ and $\bullet O_2^-$ radicals attack the methylene blue molecules adsorbed on the catalyst surface, leading to the cleavage of complex organic bonds and the gradual degradation of the dye into simpler, environmentally benign products such as CO_2 and H_2O [47]. Figure 12 illustrates the photocatalytic mechanism for Fe_2O_3@Ag/AgCl NPs of methylene dye degradation.

Table 3a. The main criteria used to determine the efficiency of Fe_2O_3@Ag/AgCl (0.03 M) for photocatalysis

No.	Time (min)	C_t	(nm)	C_t/C_0	D%	Ln (C_t/C_0)
1	0	1.559	664	1	-	0
2	15	0.404	664	0.259	74.08	-1.350
3	30	0.309	662	0.198	80.17	-1.618
4	45	0.273	661	0.175	82.48	-1.742
5	60	0.124	654	0.079	92.04	-2.531

Table 3b. The main criteria used to determine the efficiency of Fe_2O_3@Ag/AgCl (0.02 M) for photocatalysis

No.	Time (min)	C_t	(nm)	C_t/C_0	D%	Ln (C_t/C_0)
1	0	1.559	664	1	-	0
2	15	0.456	664	0.292	70.75	-1.229
3	30	0.415	663	0.266	73.38	-1.323
4	45	0.236	662	0.151	84.86	-1.887
5	60	0.209	657	0.134	86.59	-2.009

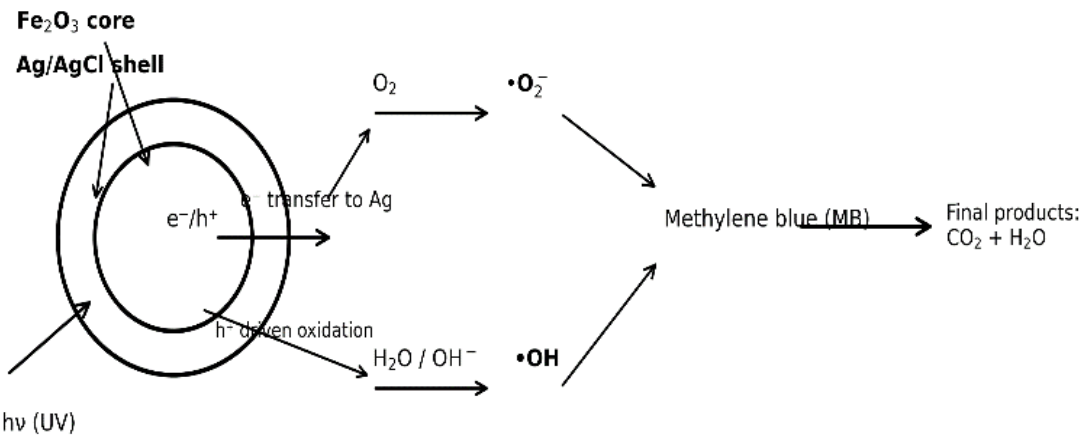

Figure 12. The photocatalytic mechanism for Fe_2O_3@Ag/AgCl NPs of methylene dye degradation

4. CONCLUSIONS

This study demonstrated that the green synthesis of Fe_2O_3@Ag/AgCl NPs using mint leaf extract is an effective and environmentally friendly approach for producing stable nanostructures. XRD results confirmed that increasing the silver nitrate concentration improved crystallinity and reduced crystallite size. EDX analysis revealed a higher content of silver and chlorine with increasing precursor concentration, confirming the formation of a thicker Ag/AgCl shell around the Fe_2O_3 core, FTIR verified the presence of organic functional groups from the extract that acted as natural stabilizing agents, while the TEM images indicate that increasing the concentration of silver nitrate leads to a thicker Ag/AgCl coating and reduces the spherical uniformity of the particles. AFM showed that higher silver content resulted in a more uniform and denser surface shell with reduced surface roughness. UV-Vis analysis demonstrated a clear increase in absorption in the ultraviolet region and a change in the optical band gap with increasing concentration of silver nitrate. The

results of the photocatalytic analysis showed that Fe_2O_3@Ag/AgCl (0.03 M) is the most effective catalyst for the degradation of methylene blue dye using ultraviolet light.

Despite the successful green synthesis of Fe_2O_3@Ag/AgCl NPs and the demonstrated superiority of the 0.03 M sample in degrading methylene blue under UV light, the study has significant limitations. The evaluation was limited to a single pollutant and conducted under controlled laboratory conditions, necessitating performance testing in real wastewater and under solar light. Furthermore, future investigations should assess long-term stability and the potential for silver/chloride leaching over extended operating cycles, and confirm the degrading mechanism using free radical capture experiments.

ACKNOWLEDGMENT

We thank the cooperation of the Nanotechnology Laboratory at the University of Baghdad, College of Science for Women, Department of Physics.

REFERENCES

[1] Malik, S., Muhammad, K., Waheed, Y.J.M. (2023). Emerging applications of nanotechnology in healthcare and medicine. Molecules, 28(18): 6624. https://doi.org/10.3390/molecules28186624

[2] Oladoye, P.O., Ajiboye, T.O., Omotola, E.O., Oyewola, O.J. (2022). Methylene blue dye: Toxicity and potential elimination technology from wastewater. Results in Engineering, 16: 100678. https://doi.org/10.1016/j.rineng.2022.100678

[3] Shishir, M.K.H., Akand, M.S., Maola, M., Monira, M.F., et al. (2025). Photocatalytic removal of textile dyes: Analytical strategies for post-degradation evaluation. Desalination, 617: 119437. https://doi.org/10.1016/j.desal.2025.119437

[4] Khan, M.A., Ahmed, M., Abu-Hussien, S.H., Zahid, M.U., Alharbi, B.F. (2025). Green synthesis of iron oxide nanoparticles (Fe_2O_3-NPs) from Citrus Limetta agrowaste for biological and photocatalytic applications. Scientific Reports, 15(1): 33107. https://doi.org/10.1038/s41598-025-17750-3

[5] Duglet, R., Sharma, D., Singh, V., Sharma, D., Singh, M. (2025). Temperature-driven evolution of hematite (α-Fe_2O_3) nanoparticles: A study on structural, morphological and magnetic properties. Solid State Communications, 396: 115761. https://doi.org/10.1016/j.ssc.2024.115761

[6] Kareem, B.A., Alshabander, B.M. (2025). Influence of pH on the photocatalytic activity of Ag/Fe_2O_3 and S/Fe_2O_3 nanoparticles by methyl blue dye degradation. Iraqi Journal of Physics, 23(2): 80-88. https://doi.org/10.30723/ijp.v23i2.1366

[7] Chakraborty, A.R., Toma, F.T.Z., Alam, K., Yousuf, S.B., Hossain, K.S. (2024). Influence of annealing temperature on Fe_2O_3 nanoparticles: Synthesis optimization and structural, optical, morphological, and magnetic properties characterization for advanced technological applications. Heliyon, 10(21): e40000. https://doi.org/10.1016/j.heliyon.2024.e40000

[8] Hossain, M.K., Mishra, A., Tiwari, A., Pant, B., et al. (2023). Thermally induced Fe_2O_3 spikes decorated Ag/Fe_2O_3 nanocomposite fabrication for anti-bacterial and anti-cancer activities. SN Applied Sciences, 5(12): 339. https://doi.org/10.1007/s42452-023-05599-y

[9] Verma, M.K., Bala, M.D., Khoza, P.B., Papo, T.R., Shozi, M.L. (2025). Core-shell nanoparticles for water purification: Advances in photocatalytic and antimicrobial applications. Next Materials, 9: 101186. https://doi.org/10.1016/j.nxmate.2025.101186

[10] Radulescu, D.M., Surdu, V.A., Ficai, A., Ficai, D., Grumezescu, A.M., Andronescu, E.J. (2023). Green synthesis of metal and metal oxide nanoparticles: A review of the principles and biomedical applications. International Journal of Molecular Sciences, 24(20): 15397. https://doi.org/10.3390/ijms242015397

[11] Obead, A.H., Abbas, N.K. (2025). Green synthesis of mgo nanoparticles via two different methods and studying their structural, morphological, and optical properties. Baghdad Science Journal, 22(8): 2638-2646. https://doi.org/10.21123/2411-7986.5027

[12] Lithi, I.J., Nakib, K.I.A., Chowdhury, A.S., Hossain, M.S. (2025). A review on the green synthesis of metal (Ag, Cu, and Au) and metal oxide (ZnO, MgO, Co_3O_4, and TiO_2) nanoparticles using plant extracts for developing antimicrobial properties. Nanoscale Advances, 7(9): 2446-2473. https://doi.org/10.1039/D5NA00037H

[13] Sarani, M., Hamidian, K., Barani, M., Adeli-Sardou, M., Khonakdar, H.A. (2023). α-Fe_2O_3@ Ag and Fe3O4@ Ag Core-Shell Nanoparticles: Green Synthesis, Magnetic Properties and Cytotoxic Performance. ChemistryOpen, 12(6): e202200250. https://doi.org/10.1002/open.202200250

[14] Goudjil, M.B., Dali, H., Zighmi, S., Mahcene, Z., Bencheikh, S.E. (2024). Photocatalytic degradation of methylene blue dye with biosynthesized Hematite α-Fe_2O_3 nanoparticles under UV-Irradiation. Desalination and Water Treatment, 317: 100079. https://doi.org/10.1016/j.dwt.2024.100079

[15] Dehdashti, F., Shirkani, H., Mehrabi, M., Ahmadi, A. (2025). Facile and green synthesis of α-Fe_2O_3 nanoparticles stabilized with chitosan for phototherapy with 808 nm laser irradiation. Scientific Reports, 15(1): 32269. https://doi.org/10.1038/s41598-025-17797-2

[16] Panchal, P., Meena, P., Nehra, S.P. (2021). A rapid green synthesis of Ag/AgCl-NC photocatalyst for environmental applications. Environmental Science and Pollution Research, 28(4): 3972-3982. https://doi.org/10.1007/s11356-020-11834-5

[17] Sharifi-Rad, M., Pohl, P. (2020). Synthesis of biogenic silver nanoparticles (Agcl-NPs) using a pulicaria vulgaris gaertn. aerial part extract and their application as antibacterial, antifungal and antioxidant agents. Nanomaterials, 10(4): 638. https://doi.org/10.3390/nano10040638

[18] Shaker, D.S., Abass, N.K., Ulwali, R.A.U. (2022). Preparation and study of the Structural, Morphological and Optical properties of pure Tin Oxide Nanoparticle doped with Cu. Baghdad Science Journal, 19(3): 24. https://doi.org/10.21123/bsj.2022.19.3.0660

[19] Madhubala, V., Kalaivani, T.J.A.S.S. (2018). Phyto and hydrothermal synthesis of Fe3O4@ ZnO core-shell nanoparticles using Azadirachta indica and its cytotoxicity studies. Applied Surface Science, 449: 584-

590. https://doi.org/10.1016/j.apsusc.2017.12.105
[20] Thanh, N.T., Maclean, N., Mahiddine, S.J.C.R. (2014). Mechanisms of nucleation and growth of nanoparticles in solution. Chemical Reviews, 114(15): 7610-7630. https://doi.org/10.1021/cr400544s
[21] Arévalo-Cid, P., Isasi, J., Caballero, A.C., Martín-Hernández, F., González-Rubio, R. (2022). Effects of shell-thickness on the powder morphology, magnetic behavior and stability of the chitosan-coated Fe_3O_4 nanoparticles. Bioactive Materials, 61(4): 300-312. https://doi.org/10.1016/j.bsecv.2020.12.001
[22] Rastgar, M., Ghasemi, Z., Samari, F. (2025). Biosynthesis of magnetic ZnO@ Fe_2O_3 nanocomposites decorated with Ag/AgCl using Hormoz Island's red soil and Avicennia marina leaf extract. Scientific Reports, 15(1): 15110. https://doi.org/10.1038/s41598-025-98442-w
[23] Yousaf, R., Zain, M., Ijaz, U. (2024). Green Synthesis and Evaluation of Mentha piperita meditated Iron Nanoparticles for in vitro Antibacterial Activity.
[24] Uma, K., Muniranthinam, E., Chong, S., Yang, T.C.K., Lin, J.H. (2020). Fabrication of hybrid catalyst ZnO nanorod/α-Fe_2O_3 composites for hydrogen evolution reaction. Crystals, 10(5): 356. https://doi.org/10.3390/cryst10050356
[25] Ahmad, S., AbdEl-Salam, N.M., Ullah, R. (2016). In vitro antimicrobial bioassays, DPPH radical scavenging activity, and FTIR spectroscopy analysis of Heliotropium bacciferum. Journal of Chemistry, 2016(1): 3818945. https://doi.org/10.1155/2016/3818945
[26] Sampaio, P.N., Calado, C.C. (2024). Enhancing bioactive compound classification through the synergy of fourier-transform infrared spectroscopy and advanced machine learning methods. Antibiotics, 13(5): 428. https://doi.org/10.3390/antibiotics13050428
[27] Pasieczna-Patkowska, S., Cichy, M., Flieger, J. (2025). Application of Fourier transform infrared (FTIR) spectroscopy in characterization of green synthesized nanoparticles. Molecules, 30(3): 684. https://doi.org/10.3390/molecules30030684
[28] Ulpathakumbura, S., Marikkar, N., Jayasinghe, L. (2023). FTIR spectral correlation with alpha-glucosidase inhibitory activities of selected leafy plants extracts. International Journal of Plant Based Pharmaceuticals, 3(1): 104-113. https://doi.org/10.29228/ijpbp.22
[29] Qi, R., Jones, D.L., Liu, Q., Liu, Q., Li, Z., Yan, C. (2021). Field test on the biodegradation of poly (butylene adipate-co-terephthalate) based mulch films in soil. Polymer Testing, 93: 107009. https://doi.org/10.1016/j.polymertesting.2020.107009
[30] Yusuf, M.O. (2023). Bond characterization in cementitious material binders using Fourier-transform infrared spectroscopy. Applied Sciences, 13(5): 3353. https://doi.org/10.3390/app13053353
[31] Mostafa, M.S., Yeasmin, S., Pranto, M.M.H., Reza, S.M., et al. (2025). Annealing-induced optimization of green-synthesized ZnO nanoparticles for improved nanopriming in sustainable agriculture. Nanoscale Advances, 7(18): 5589-5600. https://doi.org/10.1039/D5NA00354G
[32] Ahmad, S., Ni, H., Al-Mubaddel, F.S., Rizk, M.A., et al. (2025). Magnetic properties of different phases iron oxide nanoparticles prepared by micro emulsion-hydrothermal method. Scientific Reports, 15(1): 878. https://doi.org/10.1038/s41598-025-85145-5
[33] Sun, H.T., Zhou, J., Qiu, J. (2014). Recent advances in bismuth activated photonic materials. Progress in Materials Science, 64: 1-72. https://doi.org/10.1016/j.pmatsci.2014.02.002
[34] Sultana, N., Ruhul-Amin, M., Hasan, I., Kabir, S.R., Asaduzzaman, A.K.M. (2024). Antibacterial, antioxidant, and anticancer effects of green synthesized silver/silver chloride nanoparticles using Spondias pinnata bark extract. Food Chemistry Advances, 4: 100709. https://doi.org/10.1016/j.focha.2024.100709
[35] González-Hernández, A., Suárez-Domínguez, E.J., Kulich, E.F., Morales-Cepeda, A.B. (2023). Relationship analysis of surface roughness measurements on coatings using AFM and fractal dimension by mesoscopic model methods. Superficies Y Vacío, 36. https://doi.org/10.47566/2023_syv36_1-230501
[36] Graziani, G., Sassoni, E., Franzoni, E., Scherer, G.W. (2016). Hydroxyapatite coatings for marble protection: Optimization of calcite covering and acid resistance. Journal of Materials Research and Technology, 368: 241-257. https://doi.org/10.1016/j.apsusc.2016.01.202
[37] AlSultani, M.J., Alias, M.F.A. (2025). Impact of graphene oxide concentration and anthocyanin dye on the structural, morphological and optical properties of go: TiO_2 thin films. Iraqi Journal of Science, 66(6): 2336-2349. https://doi.org/10.24996/ijs.2025.66.6.12
[38] Al-Husseini, A., Sih, B., Al-Araji, A. (2021). Green synthesis of iron oxide nanoparticles (Fe_2O_3) using saffron extract. Journal of Physics: Conference Series, 2114(1): 012082. https://doi.org/10.1088/1742-6596/2114/1/012082
[39] Katubi, K.M., Jabeen, A., Alrowaili, Z.A., Shakir, I., Al-Buriahi, M.S., Warsi, M.F. (2025). The correlation of bandgap with the crystallite size using the quantum confinement effect for wastewater treatment. Desalination and Water Treatment, 322: 101115. https://doi.org/10.1016/j.dwt.2025.101115
[40] Hao, X., Wu, J., Cai, X., Li, K., Song, C., Guo, X. (2025). Plasmonic Ag-decorated GaN for efficient photothermal CO_2 conversion. Applied Catalysis B: Environmental, 373: 125366. https://doi.org/10.1016/j.apcatb.2025.125366
[41] Alharbi, M., Althubyani, H., Alarfaj, E., Dastan, D., et al. (2024). Photocatalytic performances of dip-coated Ag doped TiO_2 thin films. Archives of Metallurgy and Materials, 987-996.
[42] Xu, Y., Huang, S., Xie, M., Li, Y., et al. (2016). Core–shell magnetic Ag/AgCl@ Fe_2O_3 photocatalysts with enhanced photoactivity for eliminating bisphenol A and microbial contamination. New Journal of Chemistry, 40(4): 3413-3422. https://doi.org/10.1039/C5NJ02898A
[43] Nasri, M.S.I., Zulfiqar, M., Samsudin, M.F.R., Sufian, S., Yub Harun, N., Abdul Mudalip, S.K. (2025). Fenton-like photocatalytic oxidation and adsorption performance of MXene/g-C_3N_4 heterostructures under H_2O_2 oxidizer: Experimental & modeling approach. Discover Catalysis, 2(1): 1. https://doi.org/10.1007/s44344-025-00006-7
[44] Nazir, A., Huo, P., Wang, H., Weiqiang, Z., Wan, Y. (2023). A review on plasmonic-based heterojunction photocatalysts for degradation of organic pollutants in wastewater. Journal of Materials Science, 58(15): 6474-6515. https://doi.org/10.1007/s10853-023-08391-w

[45] Cao, A., Bai, X., Yang, C., Zhang, M. (2024). Sphere-rod-like Ag/AgCl@ Fe_2O_3 Z-scheme heterojunction as photocatalysts for efficient degradation of tetracycline under visible light irradiation. Chemosphere, 346: 140674. https://doi.org/10.1016/j.chemosphere.2023.140674

[46] Zhao, Y., Song, Y., Sun, S., Yao, S., Wang, L., Li, W., Li, S. (2024). Fabrication of multi-component heterojunction Ag/AgCl/g-C_3N_4/Sn-In_3O_2 for enhanced degradation of RhB under visible light. Journal of Water Process Engineering, 59: 105021. https://doi.org/10.1016/j.jwpe.2024.105021

[47] Matinise, N., Botha, N., Fall, A., Maaza, M. (2025). Enhanced photocatalytic degradation of methylene blue using zinc vanadate nanomaterials with structural and electrochemical properties. Scientific Reports, 15(1): 26333. https://doi.org/10.1038/s41598-025-11418-8